**FULL PAPER**

**strain** WILEY

# Constitutive equation determination and dynamic numerical modelling of the compression deformation of concrete

Semih Berk Seven[1]  |  M. Alper Çankaya[2,3]  |  Çetin Uysal[1]  |
Alper Tasdemirci[1]  |  Selçuk Saatçi[2]  |  Mustafa Güden[1]

[1]Dynamic Testing and Modeling
Laboratory, Department of Mechanical
Engineering, Izmir Institute of
Technology, Izmir, Turkey

[2]Department of Civil Engineering, Izmir
Institute of Technology, Izmir, Turkey

[3]Department of Civil Engineering, Izmir
Katip Çelebi University, Izmir, Turkey

**Correspondence**
Alper Tasdemirci, Dynamic Testing and
Modeling Laboratory, Department of
Mechanical Engineering, Izmir Institute
of Technology, Gülbahçe Köyü, Urla,
35430 Izmir, Turkey.
Email: alpertasdemirci@iyte.edu.tr

**Funding information**
Scientific and Technical Council of Turkey
(TUBITAK), Grant/Award Number:
115M534

**Abstract**

The dynamic compression deformation of an in-house cast concrete (average aggregate size of 2–2.5 mm) was modelled using the finite element (FE), element-free Galerkin (EFG) and smooth particle Galerkin (SPG) methods to determine their capabilities of capturing the dynamic deformation. The numerical results were validated with those of the experimental split Hopkinson pressure bar tests. Both EFG and FE methods overestimated the failure stress and strain values, while the SPG method underestimated the peak stress. SPG showed similar load capacity profile with the experiment. At initial stages of the loading, all methods present similar behaviour. Nonetheless, as the loading continues, the SPG method predicts closer agreement of deformation profile and force histories. The increase in strength at high strain rate was due to both the rate sensitivity and lateral inertia caused by the confinement effect. The inertia effect of the material especially is effective at lower strain values and the strain rate sensitivity of the concrete becomes significant at higher strain values.

**KEYWORDS**
concrete, LS-DYNA, pulse shaper, quartz crystal, split Hopkinson pressure bar

## 1 | INTRODUCTION

Civil engineering structures might be subjected to high loading rates due to impact and blast throughout their lifetime. Explosions at industrial or military buildings, vehicle collisions to bridge piers, rock fall to barriers in transportation structures and impact loads due to sea waves are few examples of extreme loadings on structures. Such loadings can produce high strain rates on the structure since they occur in a very short period of time.

Concrete is an essential construction material, and the dynamic behaviour is very different from quasi-static behaviour. In order to obtain sensitive and accurate analysis results of structures subjected to extreme loadings, it is important to formulate the material behaviour under high strain rates. For this purpose, many researchers have investigated the behaviour of structural materials under high strain rate conditions, including reinforced concrete.

One of the earliest investigations on the high strain rate compression of concrete was performed by Tang et al.[1] and Ross.[2] The dynamic increase factor (DIF), which is expressed as the ratio of dynamic fracture strength to static fracture strength, was found to vary between two and four. Similar DIF values were also reported by other researchers,

including the studies performed by Tang et al.[3] and Grote et al.[4] The increase of the compressive strength of concrete with increasing strain rates is ascribed to (a) strain rate-dependent tensile micro-fracture[5,6]; (b) the viscous behaviour of bulk material[6–11]; (c) the transition of deformation from uniaxial state of stress to uniaxial state of strain at increasing strain rates, leading to lateral inertia confinement[5,6,12–19]; (d) the fracture pattern dependency due to the presence of aggregates[4,12,15,20,21]; and (e) the confinement due to frictional-end effects.[5,15,22–24]

Li and Meng[25] and Zhou and Hao[20] showed that lateral inertia became dominant after about $10^2$ s$^{-1}$, while Mu et al.[26] reported that the frictional effects were responsible for the strength increment at low strains. Hao et al.[27] reported that the dynamic strength enhancement of concrete at high strain rates was resulted from the combined effects of the size of aggregates, interfacial transition zone (ITZ) and the end-frictional and lateral inertia confinement. Khosravani and Weinberg[28] reported that the dynamic compressive strength of concrete changed with aggregate size, temperature and strain rate. Flores-Johnson and Li[29] studied the structural effects on the strength increase of concrete-like materials and concluded that structural effects such as dilation, Poisson's ratio and specimen diameter might further contribute to DIF. Lee et al.[19] showed that the axial strain acceleration and the density and the geometrical properties of the concrete have affected DIF. The additional axial stress increase due to axial strain acceleration and radial confinement were also presented and formulated in several studies.[5,24,30,31]

In addition to the classical finite element (FE) methods (FEMs), the mesh-free methods have been successfully implemented into solvers and used to model the deformation of concrete. The implementation of the mesh-free methods is particularly advantageous in large deformations (crashworthiness, high-speed impact), immersed structures (concretes, reinforced composites) and moving discontinuities (crack propagation, material failure),[32] but they require relatively high CPU and memory and result in tensile instability and low-energy modes. The element-free Galerkin (EFG) method[33] is one of the earliest mesh-free methods, while the mesh-free smooth particle Galerkin (SPG)[34,35] method has been recently developed and subjected to few studies. The EFG method was implemented in LS-DYNA to improve the accuracy of solution in high gradient fields and solves the severe mesh distortion issues in large deformation problems. The main advantages of this method are its higher order of accuracy and the smoothness gathered in the solution domain.[36] The SPG method does not require mesh and instead uses particles. Most issues experienced in the meshless methods such as low-energy modes, tension instability, strain localization and excessive straining were solved to some extent in the SPG method. The low-energy modes are prevented by a penalty-based stabilisation term obtained from displacement smoothing.[37] The tension instability is lessened by applying an anisotropic updated Lagrangian kernel. The strain localization implemented by material instability is handled by a morphing algorithm. Unlike the classical FEM where the material separation is taken into account by element erosion, a bond-based material failure is introduced in SPG to create strong discontinuity in the displacement field.[38]

Tiago and Leitão[39] used the EFG formulation to analyse the damaging in the reinforced concrete beams. Xu et al.[40] used a multiscale numerical EFG method to simulate the deformation behaviour of concrete. Wu et al.[37,38,41] investigated the impact, penetration and fragmentation behaviour of concrete using SPG in LS-DYNA. Their results revealed that SPG formulation can be used to effectively simulate the material failure along with the debris evolution.

Lv et al.[42] develop a 3D meso-scale model of concrete and numerically model the split Hopkinson pressure bar (SHPB) tests of concrete specimen. In this study, aggregates, mortar and interface transition zone between them were modelled. Four typical failure patterns of concrete specimen were identified as 'slight-spalling', 'breaking', 'fragmentation' and 'comminution' through the numerical analyses. Accumulation of tensile strain damage was found to be responsible from the initiation of cracks in the loading process. Khosravani et al.[43] conducted an experimental study on ultra-high performance concrete (UHPC) using an SHPB setup at a strain rate of ~30 1/s. The SHPB setup was modified to perform spallation tests and consisted of cylindrical UHPC specimen and incident and striker bars. The dynamic elastic modulus, tensile strength and fracture energy were determined. Finally, an inverse numerical analysis was performed to verify the tests. MotahariTabari and Shooshpasha[44] employed a faster and straightforward testing method to evaluate the quality and the strength parameters of granular soil. Small and large size samples were direct shear tested, and the effects of sample size on the stress–strain, maximum shear strength, residual strength, failure envelop and volumetric behaviour of soil were analysed. The decrease in the specimen size caused the reduction of the maximum strength and residual strength after failure.

In the present study, an in-house cast concrete was tested in the SHPB setup. Afterwards, a unique numerical study was implemented in order to understand and differentiate the effects strain rate sensitivity and micro-inertia on the DIF of the tested concrete. In the numerical study, the dynamic compression deformation of the concrete under uniaxial stress state was modelled by using the classical FE, EFG and SPG methods in order to clarify the failure initiation and progression and the capabilities of each method in capturing the dynamic deformation behaviour. In all

numerical methods, the concrete was modelled using the Johnson-Holmquist concrete (JHC) material model. The constants of material model were determined through the compression tests performed both at quasi-static and high strain rates. The specimen bar interface contact forces of the SHPB tests were measured using quartz crystals. By this way, the stress equilibrium in the specimen was monitored directly. Furthermore, a thin disc of ethylene propylene diene monomer (EPDM) rubber was used as a pulse shaper in the SHPB tests. Finally, simulations were re-run by including and excluding the strain rate sensitivity effect of material.

## 2 | EXPERIMENTAL

### 2.1 | Concrete preparation and test specimens

The ingredients of the prepared concrete (cement, water and aggregates) were in accord with the ACI 211.1 code and tabulated in Table 1. The used cement was a Portland cement, CEM I 42.5R. The water/cement ratio was selected 0.4, in accord with the ACI 211.1.[45] A volume batch of 130-L concrete was prepared. The distribution of the particle size of coarse/fine aggregates and maximum aggregate size (sieve analysis) was determined by following the ASTM C136.[46] Average aggregate size was 2–2.5 mm with the maximum of 4.75 mm which is large enough to represent the bulk concrete properties and small enough not to violate approximately 1/10 ratio of aggregate size to specimen diameter ratio for the SHPB tests.[23] The concrete mixture was cast into a prismatic steel mould with the dimensions of $45 \times 45 \times 220$ mm. After the cast concrete reached sufficient strength, it was removed from the mould and kept for 28 days in water. In order to have comparable results, the geometry of cylindrical compression tests specimens was selected to be identical, and the specimens were core drilled from the moulded prismatic concrete having 39.50-mm diameter and 45-mm length. The pictures of a core-drilled plate and a strain-gaged compression test specimen are shown in Figure 1a,b.

#### 2.1.1 | Quasi-static tests

The quasi-static compression tests were performed by a 300-kN Shimadzu AG-X universal testing machine at $3.55 \times 10^{-5}$, $3.22 \times 10^{-4}$ and $2.971 \times 10^{-3}$ 1/s. The test machine and a specimen ready for the test are presented in Figure 2a. At least three specimens having an L/D ratio of 1.15 were tested at each quasi-static strain rate. Specimen surfaces were polished to avoid non-homogenous stress distribution due to surface irregularities. Force, time and cross

**TABLE 1** Ingredient and proportions of concrete

| Mixture volume (m³) | Aggregate (kg/m³) | Water (kg/m³) | Cement (kg/m³) | W/C |
|---|---|---|---|---|
| 0.13 | 1367.40 | 243.00 | 607.50 | 0.40 |



**FIGURE 1** The picture of (a) a core-drilled moulded prismatic concrete plate and a compression test specimen and (b) a strain-gaged quasi-static test specimen

head displacement (stroke) were collected directly from testing machine. However, the displacements of the test specimens were measured using a video extensometer in order to exclude test machine extension. Video extensometer followed stickers placed on the specimen, and one specimen at each strain rate was instrumented with strain gages along both vertical and horizontal direction in order to determine the Poisson's ratio.

### 2.1.2 | Dynamic tests

Dynamic compressive tests with and without pulse shaper were conducted in an SHPB setup made of 7075 T6 aluminium incident, transmitter and striker bars with 40-mm common diameter. The lengths of the incident, transmitter and striker bars were 199, 155 and 20 cm, respectively. A schematic and a view of the used SHPB setup are shown in Figures 2b and 2c, respectively. The strains on the incident and transmitter bars were measured by the full Wheatstone bridge strain gages mounted on the surfaces of the bars at a 77.5-cm distance from specimen–bar interfaces. The diameter of the concrete test specimens was very close to that of the bars (39.48 mm). Both end surfaces of the test specimens were grinded flat and sandwiched between two 10 mm thick 7075 T6 aluminium plates having the same diameter with the bars (Figure 2b). Boston Piezo-Optics X-Cut quartz crystals with a thickness of $0.25 \pm 0.01$ mm were inserted between 10 mm thick 7075 T6 aluminium plates transmitter bar and incident bar ends. The signals from the quartz crystals during the experiments were recorded by means of Kistler 5010A charge amplifiers. The piezoelectric constant of the quartz crystal was $2.3 \times 10^{-12}$ C N$^{-1}$.[47] The diameter of the crystal was chosen to be identical to the bar diameter so as to quartz crystal and aluminium bar mechanical impedances ($\rho c A$) to be very similar (aluminium bar: $14.19 \times 10^6$ kg m$^{-2}$ s$^{-1}$, quartz crystal: $15.11 \times 10^6$ kg m$^{-2}$ s$^{-1}$ with a ratio of 1.06). A Fastcam SA1.1 high-speed camera was used to record the deformation with a maximum frame rate of 675 000 fps. During the dynamic tests, each frame was captured by 37 500 fps.

In the SHPB testing of brittle materials, the pulse shaping technique is generally used in order to prevent the premature failure of specimen by imposing a gradually increasing incident wave in the test.[48,49] Note that the stress
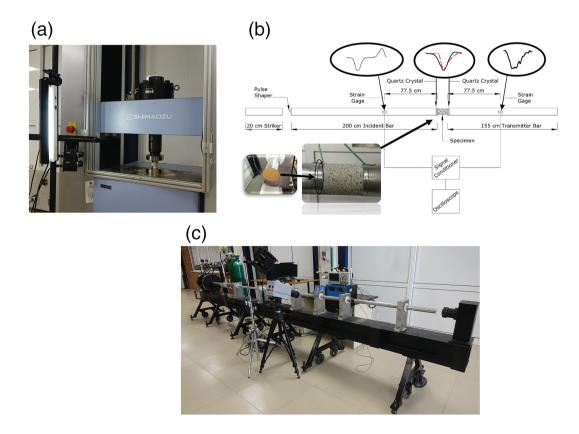


**FIGURE 2** (a) Quasi-static testing apparatus; (b) the schematic of the used SHPB setup, concrete specimen, and quartz crystal; and (c) split Hopkinson pressure bar setup

equilibrium in SHPB is established after three to four wave reverberations in the test sample.[50] If the sample fails earlier, the stress equilibrium is not attained in the sample; hence, the stress and strain equations of SHPB given earlier cannot be used. A gradually increasing incident wave delays the fracture time of specimen, hence allowing the reverberations of the incident wave in the sample to establish stress equilibrium. The material type and geometry of pulse shaper basically alter the shape of loading pulse.[51] There is a wide range of materials used for pulse shaping purposes including metals,[52] rubbers[53] and even a thin layer of paper.[54] In the current study, an EPDM rubber was used as a pulse shaper (thickness of 12.7 mm). The EPDM rubber has high deformation capabilities without fracture or rupture and remains almost circular during deformation. The determination of the size of pulse shaper is large based on the pretesting different sizes of pulse shaper in the SHPB and determining its effect on the slope of the initial rise of the incident wave. In the present study, a similar pretesting methodology was used.

In the current study, a series of experiment was conducted to see how the geometric dimensions of the pulse shaper vary the incident pulse. As seen in Figure 3, the use of pulse shaper completely removes the high-frequency oscillations in the incident stresses and an almost constant loading rate can be obtained with the appropriate dimensions. The rise time of incident bar pulse significantly increases when the thickness of the pulse shape is 3.1 mm at 20 m/s striker bar velocity. The same modifications in the incident bar stresses with the use of the pulse shaper are also seen in the same figure at higher striker bar velocities (25 and 28.6 m/s). Therefore, the thickness of the pulse shaper was selected to be 3.1 mm.

In the SHPB test, the specimen stress was calculated using the one-wave ($\sigma_{s1}$), two-wave ($\sigma_{s2}$) and three-wave stress ($\sigma_{s3}$) equations[55] as

$$\sigma_{s1} = E \frac{A}{A_s} \varepsilon_t \tag{1}$$

$$\sigma_{s2} = E \frac{A}{A_s} (\varepsilon_i + \varepsilon_r) \tag{2}$$

$$\sigma_{s3} = \frac{EA}{A_s} \left( \frac{\varepsilon_t + \varepsilon_i + \varepsilon_r}{2} \right) \tag{3}$$

where $E$ is the modulus of the bar; $A$ and $A_s$ are sequentially the area of the bar and specimen; and $\varepsilon_i, \varepsilon_r$ and $\varepsilon_t$ are the incident, reflected and transmitted waves, respectively. The specimen strain ($\varepsilon_s$) and strain rate ($\dot{\varepsilon}_s$) were calculated sequentially using the following relations.[55]

$$\varepsilon_s = \frac{c_0}{L_0} \int_0^t (\varepsilon_i - \varepsilon_t - \varepsilon_r) dt \tag{4}$$
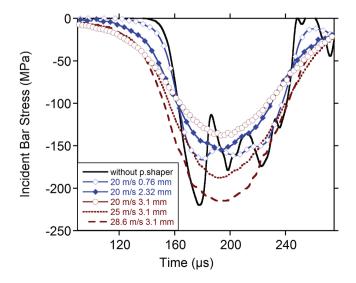


**FIGURE 3** The effect of pulse shaper geometry on the incident pulse

and

$$\dot{\varepsilon}_s = \frac{c_o}{L_o}(\varepsilon_i - \varepsilon_t - \varepsilon_r) \tag{5}$$

where $c_o$ is the elastic wave velocity of the bar material and $t$ is the time. In the SHPB tests, the stress equilibrium in the specimen is usually attained after several (at least four) stress wave reverberations.[56] The stress equilibrium parameter ($R$) is calculated as

$$R(t) = \left|\frac{\Delta\sigma(t)}{\sigma_{\mathrm{avg}}(t)}\right| = 2\left|\frac{F_1 - F_2}{F_1 + F_2}\right| \tag{6}$$

where $\Delta\sigma$ is stress difference and $\sigma_{\mathrm{avg}}$ is the average stress value between the stresses both front and back faces of the specimen. Stress is considered to be uniformly distributed as $R$ approaches zero.

# 3 | NUMERICAL MODELLING

## 3.1 | Modelling SHPB tests

Dynamic tests were modelled in non-linear FE code LS-DYNA[57] using explicit time integration method. A total of 634 200 eight-node hexahedral elements were used in the model of the SHPB setup and specimen as shown in Figure 4. The optimum mesh density was selected based on a mesh sensitivity analysis. Magnitudes and shapes of the experimentally obtained wave signals were compared with those numerically obtained for different mesh densities. These trials showed that an element size of 0.5 mm for specimen that gave an optimum result in terms of accuracy and computation time. A mesh biasing along the bar axis was also applied to refine the meshes at the contact interfaces. The specimen–bar interfaces were modelled using nodes-to-surface type contact, while the striker bar–incident bar interface was modelled using surface-to-surface type contact. The static and dynamic frictional coefficients were selected as 0.1 and 0.05, respectively. Through the numerical simulations, the incident pulse was generated in two ways. In the simulation of the tests without pulse shaper, the incident pulse was generated by the striker bar hitting the incident bar. On the other hand, in the simulations with pulse shaper, an experimentally recorded incident pulse was assigned to the incident bar front surface as a pressure function.

The SPG and EFG methods have been implemented in LS-DYNA and classical FE meshes can easily be converted into appropriate forms using the *SECTION_SOLID_SPG and *SECTION_SOLID_EFG commands, respectively. In the
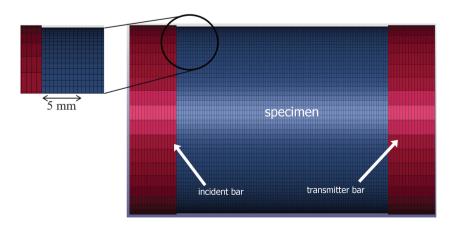


**FIGURE 4** Classical finite element modelling of a split Hopkinson pressure bar test

EFG method, the displacement is approximated by the moving least square (MLS) method and proposed by Belytschko et al.[33] The MLS approximation gives

$$u^h(X,t) = \sum_I^n \sum_j^m p_j(X)\left(A^{-1}(X,t)C(X,t)\right)_{jI} u_I(t) = \sum_I^n \phi_I(X,t)u_I(t) \tag{7}$$

where $\phi_I(X,t)$ is the shape function for node I and $u_I$ is the nodal parameter at the location $X_I$.

$$A(X,t) = \sum_I^n W(X-X_I,t)p(X_I)p^T(X_I) \tag{8}$$

$$C(X,t) = [W(X-X_1,t)p(X_1), W(X-X_2,t)p(X_2),...,W(X-X_n,t)p(X_n)] \tag{9}$$

$p$ is the linear basis function vector and $W$ is the weight function. In the EFG model, the mesh-free solid formulation was used. Nodal points are automatically converted to EFG mesh-free nodes and elements are converted to background mesh. Thus, the EFG method presents more tolerance on mesh distortion issues than the conventional FEM.

In the SPG method, due to the stability and computational efficiency, the Lagrangian mesh-free shape functions $\Psi_I(X)$ are assumed for displacement vector $u(X,t)$ as[35]

$$u^h(X,t) = \sum_{I=1}^{NP} \Psi_I(X)d_I(t) \tag{10}$$

where $NP$ is the number of mesh-free nodes and $d_I(t)$ is the nodal coefficient. The shape function is formulated as

$$\Psi_I(X) = p^T(X_I - X)q(X)\phi_a(X_I - X) \tag{11}$$

$\phi_a(X_I - X)$ is the kernel function, and in LS-DYNA, cubic B spline kernel function is used.[41] $a$ is the support size in the kernel function. $q(X)$ is an unknown vector varying with the position. $p(X_I - X)$ is the monomial basis vector. There is a bond-based failure mechanism defined in the SPG method so that the material failure and separation could be incorporated. This mechanism takes into account the interaction between the neighbouring nodes and allows the breakage of the bond if certain criteria are fulfilled. These particles are accepted disconnected as the plastic strain or stretch ratio hit their limiting values. In the classical FEM, failure is taken into account by eroding the element (sudden change in mass) and also setting the stress to zero at that particular element (sudden change in momentum).[58] In the SPG, the aforementioned bond failure mechanism preserves the change in mass and momentum. Thus, if there is more
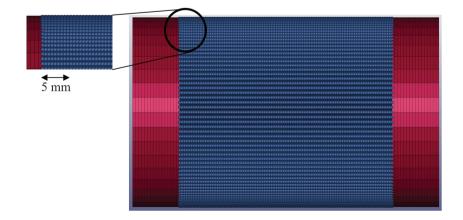


5 mm

**FIGURE 5** Element-free particle-based modelling of split Hopkinson pressure bar test

severe deformation, the SPG methodology becomes more appropriate especially where material failure and separation is available.

Both SPG and EFG particles were automatically generated using these keywords from eight-node FEM mesh of concrete used in classical model without changing the rest of the model from classical FEM model as seen in Figure 5. Contact definitions and coefficient of frictions were selected same as the FE model. Adding one simple keyword parameter which is SECTION_SPG in section card turns the FE model into SPG model in LS-DYNA. In this input, element formulation was selected as SPG. The dilation parameters of kernel function in X, Y and Z directions were selected as 1.4 with an updated Lagrangian kernel approximation. Similarly, FEM can be a converted EFG method by simply adding one more keyword card in LS-DYNA which is SOLID_EFG card in section menu. Normalised dilation parameters of the kernel function in X, Y and Z direction were selected as 1.2. Boundary conditions were coupled with FEM/EFG method with essential boundary condition treatment (IEBT) = 3. The two-point Gauss integration method was selected.

## 3.2 | Johnson–Holmquist concrete material model

The specimen was modelled using the JHC pressure and strain rate sensitive model.[59] The model is well suited for the concrete exposed to relatively high pressures and strain rates with large strains. The model was integrated into LS-DYNA as MAT_JOHNSON_HOLMQUIST_CONCRETE (*MAT_111), and there are 19 material model parameters for mechanical properties, strength parameters, equation of state, damage and strain rate sensitivity. The strength, damage and the hydrostatic pressure–volume relationship of the model are shown sequentially in Figure 6a–c. The constitutive behaviour is defined as

$$\sigma^* = \left[A(1-D) + BP^{*N}\right]\left[1 + Cln\dot{\epsilon}^*\right] \leq Smax \tag{12}$$

where $\sigma^*$, $P^*$ and $T^*$ are the normalised equivalent stress, pressure and tensile strength respectively; $f'_c$ is the unconfined uniaxial compressive strength; $\sigma$ stands for the actual equivalent stress and $P$ is the actual pressure; and $\dot{\epsilon}^* = \dot{\epsilon}/\dot{\epsilon}_0$ is the dimensionless strain rate where instantaneous strain rate ($\dot{\epsilon}$) is normalised by reference strain rate ($\dot{\epsilon}_0$). $Smax$ is the
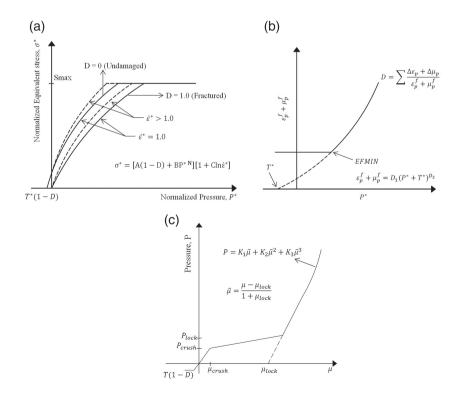


**FIGURE 6** (a) The strength–pressure, (b) damage–pressure and (c) the pressure–compaction behaviour of the JHC model[59]

normalised maximum strength of concrete. $A$, $B$ and $N$ are the material constants and sequentially named as the normalised cohesive strength, the normalised pressure hardening coefficient and the pressure hardening exponent. $C$ is the strain rate sensitivity parameter and $D$ ($0 \leq D \leq 1$) is the accumulated damage.

The material damage in the JHC model is the accumulation of strain. Both equivalent plastic strain and plastic volumetric strain are controlling damage parameter. Damage is defined as

$$D = \sum \frac{\Delta \varepsilon_p + \Delta \mu_p}{\varepsilon_p^f + \mu_p^f} \tag{13}$$

where $\Delta \varepsilon_p$ is equivalent plastic strain increment and $\Delta \mu_p$ is volumetric plastic strain increment. $\varepsilon_p^f + \mu_p^f = f(P)$ is the total plastic strain to fracture and it is defined as

$$\varepsilon_p^f + \mu_p^f = D_1 (P^* + T^*)^{D_2} \geq \varepsilon_p^f min \tag{14}$$

where $D_1$ and $D_2$ are damage constants. $T^*$ is the normalised hydrostatic tensile strength. $\varepsilon_p^f min$ (EFMIN) is also a damage constant initiating the fracture of the material at a certain plastic strain. The pressure–compaction curve is generally divided into three distinct phases (Figure 6c). The first phase *(OA)* is the linear elastic region ranging from the negative pressure to the elastic limit, $P_{crush}$. The second phase *(AB)* is referred as the transitional region. At this stage, the air voids are progressively compressed out of the concrete and the compaction damage occurs until reaching the point ($\mu_{lock}$, $P_{lock}$). The third phase *(BC)* is the compaction region at which all air voids are removed from concrete and is assumed non-linear elastic.

# 4 | RESULTS AND DISCUSSION

## 4.1 | The effect of pulse shaping and compression strength

The incident, reflected and transmitter bar responses of three tests in the SHPB with pulse shaper at 20 m/s striker bar velocity are shown in Figure 7. As seen in the same figure, the separate tests at the same striker bar velocity result in very much similar stress waves on the bars, showing the repeatability of the tests with pulse shaper.

The experimental stress–strain curves of the concrete calculated from one-wave, two-wave and three-wave analyses of the SHPB and from the quartz crystal between the specimen/transmitter bar interface are shown in Figure 8 for pulse shaper tests. With the insertion of quartz crystals at the specimen/bar interfaces, the force history over the cross-sectional area of the specimen was directly measured from the interfaces. In the indirect surface strain measurements (data collected from the strain gages), the strain on the bar surface is assumed to be the same as at the specimen/bar interfaces when two basic conditions are met: (i) the wave propagation within the bars is one-dimensional, and (ii) the specimen deforms uniformly.[60] These assumptions may not generally be satisfied since the specimen is generally
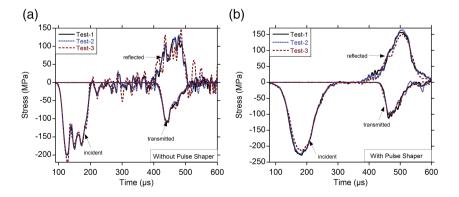


**FIGURE 7** The bar responses of split Hopkinson pressure bar tests of concrete (a) without and (b) with pulse shaper at 20 m/s
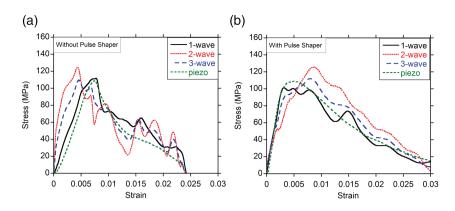
**FIGURE 8** Stress wave analysis of the experimental split Hopkinson pressure bar data (a) without and (b) with pulse shaper

smaller in diameter than the bar resulting in that the bar ends are not uniformly loaded across the cross-sectional area.[61] In addition, materials like concrete consisting of vastly different behaving constituents may locally indent the bar ends. In the testing of concrete, generally bigger diameter bars are preferred due to the limitations of the minimum specimen size.[62,63] The different frequencies of pulses induced in the bars disperse with the distance travelled in the bar and the amount of dispersion also increases as the diameter of the bar increases; thus, the wave dispersion effects become more pronounced. These wave dispersion effects cause large oscillations in the acquired signals.[64,65] The placement of quartz crystals at the bar interfaces is mainly due to overcoming the aforementioned drawbacks of the classical SHPB testing methodology in the testing of concrete.

The discrepancies between the stress–strain curves of one-wave, two-wave and three-wave analyses in the same figure arise from the oscillating and dispersive nature of the incident and reflected waves. Since the two-wave analysis includes incident and reflected waves and three-wave analysis all three waves, it is expected that two-wave and three-wave analyses follow quite different trend from the one-wave analysis due to non-equilibrium stress state in the specimen. The stress calculated from the strain gages (indirect measurement) is more oscillatory from the quartz crystal for the tests without and with pulse shaper. The difference between the force values obtained from bars and quartz crystals is reduced significantly when a pulse shaper is used. Figure 9a shows the variations of the strain rate with time in the test with and without pulse shaper. Within the strain range of the maximum stress (0.0042–0.007), the strain rate fluctuates between a high (326 1/s) and a low value (200 1/s) in the test without a pulse shaper, while the strain rate is nearly constant (∼240 1/s) in the test with the pulse shaper (Figure 9a). The variations of R with strain are also shown in Figure 9b for both tests. An earlier and less oscillatory stress equilibrium is attained in the test with pulse shaper. The stress equilibrium is reached before the failure strain of the concrete specimen in the tests with pulse shaper.

The representative stress–strain curves at the quasi-static strain rates and at the dynamic strain rate using pulse shaper are shown in Figure 10a. The maximum stress is taken as the compressive strength as marked by arrows in the
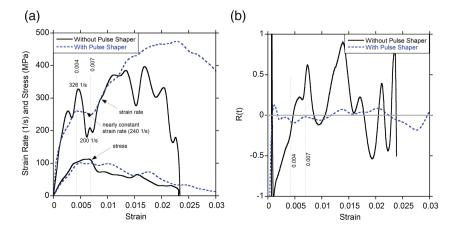


**FIGURE 9** Strain–strain rate and stress equilibrium parameter (a) without and (b) with pulse shaper
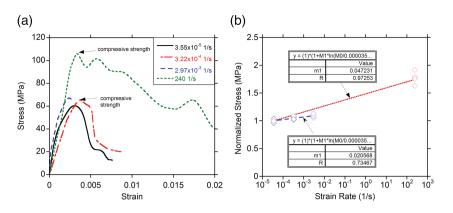
**FIGURE 10** (a) Representative stress–strain curves at different strain rates and (b) the normalised compressive strength versus strain rate

same figure. As the strain rate increases at the quasi-static strain rates, the compressive strength increases. The average compressive strength was sequentially $62 \mp 3$, $64.9 \mp 3$ and $67.5 \mp 3$ MPa for $3.55 \times 10^{-5}$, $3.22 \times 10^{-4}$ and $2.971 \times 10^{-3}$ 1/s. A sharp increase in the compressive strength ($109.7 \mp 10$ MPa) is found when the strain rate increases from quasi-static to dynamic strain rate, 240 1/s. The variation of the normalised compressive strength (compressive strength/compressive strength at $3.55 \times 10^{-5}$ 1/s) with logarithm of the strain rate is shown in Figure 10b. Fitting all the compressive strength values and only quasi-static strain rate compressive strength values with Equation 12 gives sequentially 0.047 and 0.02 for the strain rate sensitivity parameter ($C$) as shown in Figure 10b. Clearly, the quasi-static strain rate compressive strength data show a lower strain rate sensitivity than the compressive strength at all strain rates investigated.

In both quasi-static and dynamic tests, cracks form on the tested specimen at a strain corresponding to the compressive strength (Figures 11 and 12). The cracks follow the same direction with the loading axis. The average crack lengths were measured optically using ImageJ[66] software and the values were determined $9.6 \mp 3$ and $5.2 \mp 1.1$ mm for quasi-static and dynamic tests, respectively. Although the lengths of the cracks in the quasi-static test are longer than those in
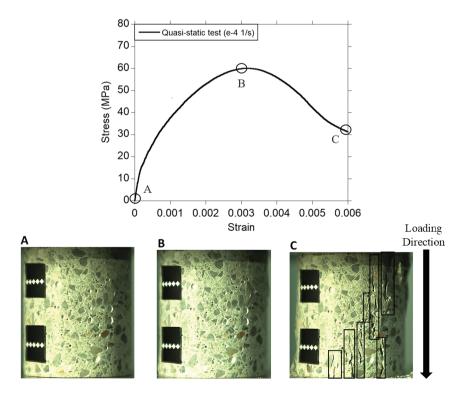


**FIGURE 11** Deformation and failure behaviour of concrete in the quasi-static strain rate test

the dynamic test, the number of cracks is higher in the dynamic test at the failure strain. Since there is less time for the crack to grow in the dynamic test, several micro-cracks initiate simultaneously. These micro-cracks pass through the aggregates as shown in Figure 12, which may cause dynamic strength increase of the concrete at high strain rates. In this figure, the photos were captured by 37 500 fps.

## 4.2 | Material model parameters determination

The density of the concrete specimen was found to be 2183 kg/m$^3$. Uniaxial compressive strength ($f'_c$) of concrete was $62 \pm 3$ MPa at the lowest strain rate which is also reference strain rate, $3.554 \times 10^{-5}$ s$^{-1}$. The Poisson's ratio was obtained from quasi-static tests as 0.2 in average. Elastic modulus was found by taking the slope of stress strain curve of a quasi-static test up to 0.45 $f'_c$. Shear and elastic bulk modulus were both calculated using the following equations: $G = E/2(1+v)$ and $K_{elastic} = E/3(1 - 2v)$. The maximum tensile hydrostatic pressure was found using split tensile test result which is 6.3 MPa; normalising to $f'_c$ gives $T*$ is equal to 0.102.

Equation 12 can be simplified with the elimination of strain rate and damage effects, and the equivalent stress in this case can be constituted as[67]

$$\sigma^* = \left[A + BP^{*N}\right] \tag{15}$$

In Equation 15, the strength parameters $A$, $B$ and $N$ were determined using a fit through normalised pressure-normalised equivalent stress curve in Figure 13. The data in the lower bound of pressures $0 < P^* < 1$ were provided within the quasi-static and high strain rate tests. Higher pressure data were taken from the study by Ren et al.[67] where the tests were carried out by Xiong[68] ($1 < P^* < 4$). The compressive strength of the tested concrete in Xiong's work (61 MPa) was very close to the concrete used in the current study (62 MPa). The maximum normalised stress, *Smax*, was selected as 7.0, the same as with the Holmquist et al.[59] due to the unavailable data at higher pressures. The
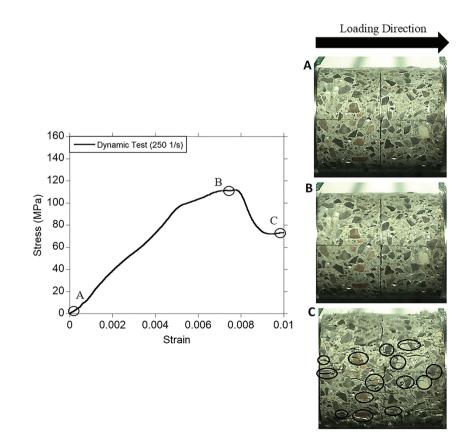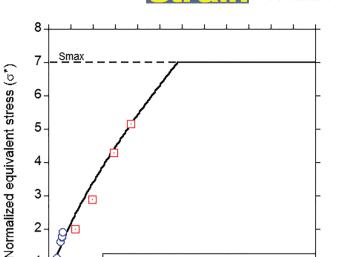


**FIGURE 12** Deformation and failure behaviour of concrete in the high strain rate test

FIGURE 13　Determination of strength parameters



normalised cohesive strength was determined as 0.25 which is the point where normalised equivalent stress intersects the axis when $P^* = 0$. Setting $B = 1.96$ and $N = 0.70$ gives a good fit with the experimental data as shown in Figure 13. A similar study was also done by Ren et al.[67] Using the available data in quasi-static, triaxial compression and SHPB tests in the literature, they found that $A = 0.30$, $B = 1.73$, $N = 0.79$ and $C = 0.005$; these values are within the comparable margins when the parameters found in the current study are concerned.

In the dynamic testing of brittle materials, there is greater amount of variance between the results reported by the researchers even for the very similar type of materials. It is very important to correctly determine the actual strain rate sensitivity of the material. Generally, as the loading rate increases especially under compression, the strength increase may not be only due to the intrinsic rate sensitivity of the material but may be due to some other effects such as the hydrostatic pressure formation which is resulting in a lateral confinement effect in the specimen. Thus, the hydrostatic pressure effects need to be eliminated. To do that, five tests at different strain rates are considered as shown in Figure 14. As suggested by Holmquist et al.,[59] a straight line was drawn from $T^* = 0.102$ to the corresponding
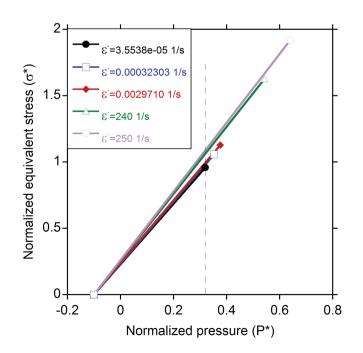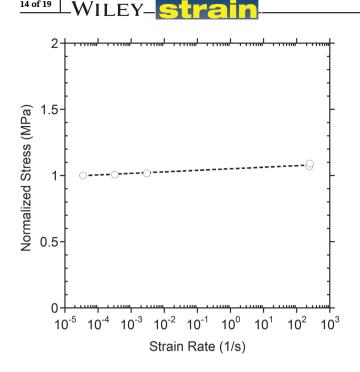


FIGURE 14　Elimination of hydrostatic pressure

**FIGURE 15** Determination of strain rate parameter

equivalent stresses at each strain rates. Then, the intersection points on the line drawn from $P^* = 1/3$ were taken as normalised equivalent stresses without the hydrostatic pressure effect (Figure 14). Normalised equivalent stress values without the hydrostatic pressure effect as a function of corresponding strain rate were fitted using the least square fit method as shown in Figure 15 and strain rate parameter $C$ was determined as 0.005. The determined JHC material model constants of the concrete material are tabulated in Table 2.

## 4.3 | Numerical results

The SHPB test experimental and numerical bar responses of the sample with pulse shaper are shown in Figure 16a. The numerical bar responses are obtained with three distinct approaches which are FEM, SPG and EFG as mentioned earlier. Both experimental and numerical bar response histories are in a good agreement overall. The maximum stress in the transmitted wave corresponds to the point of fracture of the specimen. When pulse shaper is used, a slowly rising incident pulse is produced experimentally and numerically allowing the minimization of the dispersive effects and an earlier dynamic stress equilibrium in the specimen. The experimental stress–strain curves determined from the bar strain gage and piezoelectric crystal and the numerical stress–strain curves of the investigated three numerical methods are shown in Figure 16b for comparison. The experimental bar curve in the figure represents the stress calculated from Equation 1, while the experimental piezo curve represents the stress calculated from the measured force data of the piezoelectric rystal. Both EFG and FE methods overestimated the failure stress and strain values of concrete specimen. On the other hand, while the SPG method underestimates the peak stress value, it gives very close failure stress and strain values. Also, SPG simulation showed similar load capacity profile with the experiment causing fully damaged

**TABLE 2** The material model constants

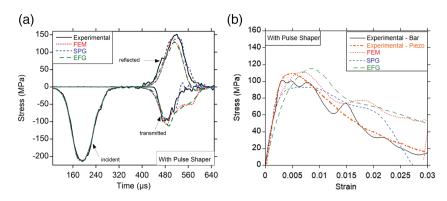| Strength constants | $A$ | $B$ | $N$ | $C$ | $f'_c$ (MPa) | $Smax$[49] | $G$ (GPa) | - |
|---|---|---|---|---|---|---|---|---|
| | 0.25 | 1.96 | 0.70 | 0.005 | 62 | 7.0 | 13.32 | |
| Damage constants | $D_1$[49] | $D_2$[49] | $\varepsilon_p^f$ | - | - | - | - | - |
| | 0.04 | 1.0 | 0.01 | | | | | |
| Pressure constants | $P_{crush}$ (GPa) | $\mu_{crush}$ | $K1$[49] (GPa) | $K2$[49] (GPa) | $K3$[49] (GPa) | $P_{lock}$[49] (GPa) | $\mu_{lock}$ | $T$ (GPa) |
| | 0.0210 | 0.001 | 85 | −171 | 208 | 0.80 | 0.173 | 0.0063 |

**FIGURE 16** Numerical and experimental (a) bar responses and (b) stress–strain curves in split Hopkinson pressure bar test with pulse shaper

specimen at 0.025 strain. It can also be concluded that EFG and FE method simulations give extra stiffness to the specimen causing longer load capacity of the specimen unlike the SPG method.

## 4.4 | Dynamic strength enhancement of concrete

In order to understand the significance of lateral inertia, the numerical model of the SHPB test was re-run with identical conditions and definitions but the strain rate sensitivity parameter defined or assumed zero. This way, the contributions of lateral inertia and the intrinsic rate sensitivity of the material on the dynamic strength increase could be calculated numerically and are presented in Figure 17a,b for the tests without and without pulse shaper. In the material model, a strain rate sensitivity parameter determined within the quasi-static strain rate range experimental strength data, $C = 0.005$, was used. The difference between the stress values determined numerically by taking
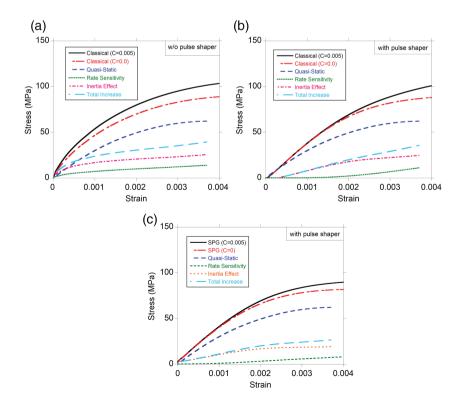


**FIGURE 17** Effect of strain rate sensitivity and inertia: (a) without (finite element method), (b) with pulse shaper (finite element method) and (c) with pulse shaper (smooth particle Galerkin )

$C = 0.005$ and $C = 0$ gives the effect of strain rate on the dynamic stress values individually. On the other hand, the effect of lateral inertia was calculated by taking the difference between the stress–strain curves of the numerical simulation with $C = 0$ and the experimental quasi-static test. The strength increase due to the strain rate sensitivity in the test without pulse shaper is 14 MPa and due to the inertia is 25 MPa at the failure strain (Figure 17a). In the test with pulse shaper, the strength increase due to the strain rate sensitivity and inertia is 11 and 25 MPa at the failure, respectively (Figure 17b). The effect of lateral inertia in the pulse shaper test is found to be close to that in the without pulse shaper test, while the effect of strain rate is more pronounced in the test without pulse shaper. It was also observed that there was a strength increase by the strain rate even at low strains (0.002) in the test without pulse shaper. However, the
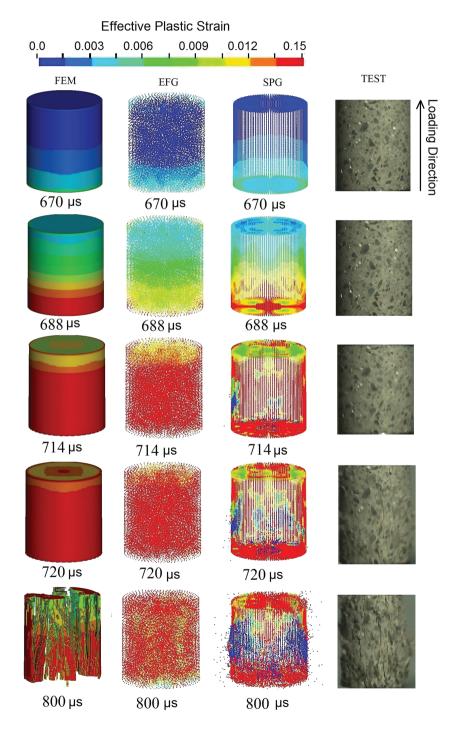


**FIGURE 18** The maximum principle strain contours of the specimen at different times for finite element, element-free Galerkin and smooth particle Galerkin models along with the experimental results

strength increase due to strain rate sensitivity arises after 0.002 strain in the test with pulse shaper. Based on the numerical analysis results, two main effects are found for the strain rate sensitivity: (i) the inertia effect of the material itself especially effective at lower strain values and (ii) the strain rate sensitivity of the concrete itself which becomes significant at higher strain values. Coupling experimental and numerical results allowed to identify the contributions of these effects individually. Results have proved similar inertia contributions for with and without pulse shaper tests. Figure 17a,b was drawn using FEM data, whereas Figure 17c was obtained using the SPG numerical results. As can be seen from the figure, both methodologies give consistent results. When the pulse shaper is used, the increasing rate of strain rate is lower when it is compared with that of without pulse shaper, resulting in lower rate sensitivity behaviour especially at lower strain values.

The deformation behaviour of concrete changes as the strain rate increases. It was stated that the distinctive behaviour of these materials under different loading conditions was due to the microstructure of ceramic.[56] Cui et al.[69] pointed out that the weakest bond in concrete is the aggregate and mortar interface. Thus, failure initiates at these areas under static loading conditions. However, there is no time for cracks to find the weakest location under dynamic loading conditions; instead, a higher number of cracks simultaneously occur at relatively high strength regions (i.e., aggregates itself). Hao et al.[70] stated that the presence of aggregates in concrete is one of the main reasons in the dynamic strength enhancement of concrete at high strain rates.

Figure 18 presents the specimen maximum principal strain contours of different solution methodologies at various times. After the arrival of the stress wave to the specimen front surface, the specimen is loaded. At the initial stage, the specimen is elastically loaded and a tensile strain due to the Poisson effect localises at the specimen front and side surfaces. As the deformation continues, the tensile strain increases at the front surface of the specimen and the damage initiates at this location and propagates through the lateral and radial directions of the specimen. At a later stage of loading, the stress wave almost travels through the specimen and damage becomes accumulated on the side surface of the specimen. Due to the further loading/compression of the specimen, large amounts of damage localise, and catastrophic failure occurs with the fragmentation of the specimen. As can be seen from the figure for the initial stages of the deformation, all three numerical solution routes give similar results. However, as the deformation increases, SPG gives more realistic results and close deformation profiles as far as the experimental results are concerned. FEM results deviate from the experimental results in terms of both force histories and damage contours at the later stages of deformation.

# 5 | CONCLUSIONS

The results showed that both EFG and FE methods overestimated the failure stress and strain values of concrete, while the SPG method underestimated the peak stress value. SPG simulation showed similar load capacity profile with the experiment causing fully damaged specimen at 0.025 strain. At initial stages of the loading, FE, EFG and SPG methods present similar behaviour. Nonetheless, as the loading continues, the SPG method predicts closer agreement of deformation profile and force histories as far as the experimental data are concerned. The difference from the experimental results in terms of both force histories and damage contours at the later stages of deformation increases as the deformation continues. The failure mechanisms and deformation profiles observed both experimentally and numerically are in good agreement with the study of Lv et al.[42] They reported four different failure patterns depending on the strain rates attained during the test: slight-spalling, breaking, fragmentation and comminution. The numerical results also showed that the increase in strength at high strain rate was due to both the strain rate sensitivity and lateral inertia caused by the confinement effect. From these two effects, the inertia effect of the material itself especially is effective at lower strain values and the strain rate sensitivity of the concrete itself becomes significant at higher strain values. The contribution of the inertia effect level is again in close agreement with that observed by Zhou et al.[20] They also showed that the effect of inertia increases as the strain rate increases. High-speed camera recordings showed that micro-cracks occurred in the dynamic test and these cracks followed a path passing through relatively higher strength aggregates rather than the weakest bond between the aggregates and mortar. This behaviour may also be attributed to the dynamic strength enhancement of concrete.

## ORCID

*M. Alper Çankaya* https://orcid.org/0000-0002-5491-3425
*Alper Tasdemirci* https://orcid.org/0000-0002-2926-0661
*Mustafa Güden* https://orcid.org/0000-0001-6397-8418

## REFERENCES

[1] T. X. Tang, L. E. Malvern, D. A. Jenkins, Proceedings of second symposium on the interaction of non-nuclear munitions with structures, **1985**, 194.

[2] C. A. Ross, *DTIC* **1989**, 88.

[3] T. Tang, L. E. Malvern, D. A. Jenkins, *Journal of Engineering Mechanics* **1992**, *118*(1), 108.

[4] D. L. Grote, S. W. Park, M. Zhou, *International Journal of Impact Engineering* **2001**, *25*, 869.

[5] P. H. Bischoff, S. H. Perry, *Materials and Structures* **1991**, *24*, 425.

[6] J. Ožbolt, A. Sharma, *Engineering Fracture Mechanics* **2012**, *85*, 88.

[7] P. Rossi, *Magazine of Concrete Research* **1991**, *43*, 53.

[8] P. Rossi, J. G. M. van Mier, C. Boulay, F. Le Maou, *Materials and Structures* **1992**, *25*, 509.

[9] D. Yan, G. Lin, *Cement and Concrete Research* **2006**, *36*, 1371.

[10] P. Rossi, J. G. M. Van Mier, F. Toutlemonde, F. Le Maou, C. Boulay, *Materials and Structures* **1994**, *27*, 260.

[11] C. A. Ross, D. M. Jerome, J. W. Tedesco, M. L. Hughes, *ACI Mater. J.* **1996**, *93*, 293.

[12] Y. Hao, H. Hao, X. H. Zhang, *International Journal of Impact Engineering* **2012**, *39*(1), 51.

[13] Y. Hao, H. Hao, *Advances in Structural Engineering* **2016**, *19*, 1027.

[14] H. Le Nard, P. Bailly, *Mechanics of Cohesive-frictional Materials* **2000**, *5*, 491.

[15] Y. Hao, H. Hao, *Construction and Building Materials* **2013**, *48*, 521.

[16] M. Zhang, H. J. Wu, Q. M. Li, F. L. Huang, *International Journal of Impact Engineering* **2009**, *36*, 1327.

[17] Q. M. Li, Y. B. Lu, H. Meng, *International Journal of Impact Engineering* **2009**, *36*, 1335.

[18] J. Cui, H. Hao, Y. Shi, *Construction and Building Materials* **2018**, *171*, 839.

[19] S. Lee, K. M. Kim, J. Park, J. Y. Cho, *International Journal of Impact Engineering* **2018**, *113*, 191.

[20] X. Q. Zhou, H. Hao, *International Journal of Solids and Structures* **2008**, *45*, 4648.

[21] Y. Hao, H. Hao, Z. X. Li, *International Journal of Protective Structures* **2010**, *1*(1), 145.

[22] T. Iwamoto, T. Yokoyama, *Mechanics of Materials* **2012**, *51*, 97.

[23] Q. B. Zhang, J. Zhao, *Rock Mechanics and Rock Engineering* **2014**, *47*, 1411.

[24] M. Hassan, K. Wille, *Construction and Building Materials* **2017**, *144*, 747.

[25] Q. M. Li, H. Meng, *International Journal of Solids and Structures* **2003**, *40*, 343.

[26] Z. C. Mu, A. N. Dancygier, W. Zhang, D. Z. Yankelevsky, *International Journal of Impact Engineering* **2012**, *49*, 91.

[27] Y. Hao, H. Hao, Z. X. Li, *International Journal of Impact Engineering* **2013**, *60*, 82.

[28] M. R. Khosravani, K. Weinberg, *Construction and Building Materials* **2018**, *190*, 1264.

[29] E. A. Flores-Johnson, Q. M. Li, *International Journal of Impact Engineering* **2017**, *109*, 408.

[30] A. R. Naghdabadi, M. J. Ashrafi, *Constr. Build. Mater.* **2016**, *125*, 326.

[31] T. Chen, Q. B. Li, J. F. Guan, *Applied Mechanics and Materials* **2013**, *438-439*, 215.

[32] C. T. Wu, Y. Guo, W. Hu, 13th International LS-DYNA Users Conference. **2014**, 1.

[33] T. Belytschko, Y. Y. Lu, L. Gu, *International Journal for Numerical Methods in Engineering* **1994**, *37*, 229.

[34] C. T. Wu, S. W. Chi, M. Koishi, Y. Wu, *International Journal for Numerical Methods in Engineering* **2016**, *107*(1), 3.

[35] C. T. Wu, M. Koishi, W. Hu, *Computational Mechanics* **2015**, *56*(1), 19.

[36] C. Wu, M. Botkin, H.-P. Wang, 7th International LS-DYNA Users Conference, **2002**.

[37] C. T. Wu, Y. Wu, J. E. Crawford, J. M. Magallanes, *International Journal of Impact Engineering* **2017**, *106*, 1.

[38] Y. Wu, D. Wang, C. T. Wu, *Theoretical and Applied Fracture Mechanics* **2014**, *72*, 89.

[39] C. M. Tiago, V. M. A. Leitão, *Comput. Struct.* **2004**, *82*, 1503.

[40] Q. Xu, J. Chen, J. Li, *International Journal of Mechanics and Materials in Design* **2012**, *8*, 113.

[41] Y. Wu, D. Wang, C. T. Wu, H. Zhang, *International Journal of Impact Engineering* **2016**, *87*, 169.

[42] T. H. Lv, X. W. Chen, G. Chen, *Construction and Building Materials* **2018**, *160*, 744.

[43] M. R. Khosravani, P. Wagner, D. Fröhlich, K. Weinberg, *Eng. Struct.* **2019**, *201*, 109844.

[44] S. MotahariTabari, I. Shooshpasha, *Int. J. Geotech. Eng.* **2018**, 1.

[45] G. Donald, D. E. Dixon, J.R. Prestrera, *ACI* **2002**, 1.

[46] ASTM. **2014**.

[47] B. P. Optics, Material Properies of Crystal Quartz.

[48] D. J. Frew, M. J. Forrestal, W. Chen, *Experimental Mechanics* **2001**, *41*(1), 40.

[49] D. J. Frew, M. J. Forrestal, W. Chen, *Experimental Mechanics* **2002**, *42*(1), 93.

[50] G. Ravichandran, G. Subhash, *Journal of the American Ceramic Society* **1994**, *77*(1), 263.

[51] K. Xia, W. Yao, *Journal of Rock Mechanics and Geotechnical Engineering* **2015**, *7*(1), 27.

[52] *Proceedings of the Royal Society of London. Series A: Mathematical and Physical Sciences* **1991**, *435*, 371.

[53] W. Chen, B. Zhang, M. J. Forrestal, *Experimental Mechanics* **1999**, *39*, 81.

[54] X. J. Wu, D. A. Gorham, *Le Journal de Physique IV* **1997**, *07*, C3.

[55] B. A. Gama, S. L. Lopatnikov, J. W. Gillespie, *Applied Mechanics Reviews* **2004**, *57*, 223.

[56] G. Subhash, G. Ravichandran, *ASM Handbook: Mechanical Testing and Evaluation* **2000**, *8*, 497.

[57] Livermore Software Technology Corporation, *LS-DYNA keyword user's manual* **2016**, *II*, 1.

[58] Y. Wu, C. T. Wu, W. Hu, *FEA Information Engineering Journal* **2019**, *8*, 4.

[59] T. J. Holmquist, G. R. Johnson, W. H. Cook, 14th International Symposium, **1993**, *2*, 591.

[60] S. Nemat-Nasser, Introduction to high strain rate testing, in mechanical testing and evaluation. ASM International, H. Kuhn, D. Medlin, **2000**.

[61] G. T. Gray III, Classic split-Hopkinson pressure bar testing, in mechanical testing and evaluation. ASM International, H. Kuhn, D. Medlin, **2000**.

[62] P. Zhao, T. S. Lok, *Structural Engineering and Mechanics* **2005**, *19*, 603.

[63] R. Merle, H. Zhao, *International Journal of Impact Engineering* **2006**, *32*, 1964.

[64] T. S. Lok, X. B. Li, D. Liu, P. J. Zhao, *Journal of Materials in Civil Engineering* **2002**, *14*, 262.

[65] F. Yang, H. Ma, L. Jing, L. Zhao, Z. Wang, *Latin American Journal of Solids and Structures* **2015**, *12*, 730.

[66] W. Rasband, ImageJ. National Institutes of Health, USA.

[67] G. M. Ren, H. Wu, Q. Fang, X. Z. Kong, *International Journal of Protective Structures* **2017**, *8*, 352.

[68] Y. B. Xiong, *Research on constitutive parameters of concrete based on the Johnson-Holmquist concrete model*, **2009**.

[69] J. Cui, H. Hao, Y. Shi, *International Journal of Impact Engineering* **2017**, *106*, 202.

[70] Y. Hao, H., Hao, *International Journal of Protective Structures* **2011**, *2*, 177.